Direct prediction of electrical properties of grain boundaries from photoluminescence profiles using machine learning

View Online   Export Citation   CrossMark

Kentaro Kutsukake,[1,a)] (iD) Kazuki Mitamura,[2] (iD) Noritaka Usami,[2] (iD) and Takuto Kojima[3] (iD)

AFFILIATIONS

[1]Center for Advanced Intelligence Project, RIKEN, Tokyo 103-0027, Japan
[2]Graduate School of Engineering, Nagoya University, Nagoya 464-8603, Japan
[3]Graduate School of Informatics, Nagoya University, Nagoya 464-8603, Japan

[a)]Author to whom correspondence should be addressed: kentaro.kutsukake@riken.jp

ABSTRACT

We present a machine learning model to directly predict the carrier recombination velocity, v_{GB}, at the grain boundary (GB) from the measured photoluminescence (PL) intensity profile by training it with numerical simulation results. As the training dataset, 1800 PL profiles were calculated with a combination of random values of four material properties—v_{GB}, the GB inclination angle, and the carrier diffusion lengths in the grains on both sides of the GB. In addition, the measured noise was modeled artificially and applied to the simulated profiles. A neural network was constructed with the inputs of the PL profile and the outputs of the four properties. This served as the solver of the reverse problem of the computational simulation. The coefficient of determination and the root mean squared error of v_{log}, which is the common logarithm of v_{GB}, for the test dataset were 0.97 and 0.245, respectively. This prediction error was sufficiently low for the practical estimation of v_{GB}. Moreover, the calculation time was reduced by a factor of 198 000 compared to conventional numerical optimization of repeating the computational simulations. By utilizing this fast prediction method, continuous evaluation of v_{GB} along a GB was demonstrated. The finding is expected to advance scientific investigation of the electrical properties of local defects.

Published under an exclusive license by AIP Publishing. https://doi.org/10.1063/5.0049847

Experimental measurements are generally performed on materials to determine their properties, such as electrical, optical, magnetic, and mechanical properties. In some cases, the desired property may not be determined directly from the measurement data. In such cases, computational simulations that model the physical and measurement systems are used to determine the material properties. Figure 1(a) shows a schematic of the process for evaluating the electrical property of the grain boundary (GB) through carrier and optical simulation using photoluminescence (PL) image measurement as an example. A computational simulation solves the governing equations and yields a spatial distribution of the excess carrier density. The physical properties are incorporated into the model as parameters of the governing equations and boundary conditions. Subsequently, a measurable PL intensity profile is calculated from the distribution of the carrier density by simulating the luminescence and measurement systems. Thus, if the series of simulations is handled as a function, the inputs are the physical properties and the outputs are the measurable PL intensity profiles.

To assess the physical property values from the measurement data, the reverse problem of the simulations must be solved. Generally, this reverse problem is solved by optimizing the simulation output onto the measurement data. Many optimization methods are used to evaluate material properties, including the gradient method,[1–3] genetic algorithm,[4] and Bayesian optimization.[5] However, these optimization methods require repeated calculations of the simulations, which increase the calculation costs.

Recently, machine learning (ML) has been applied to materials research simulations. One application is a surrogate model[6] for high-cost computational simulations, such as computational fluid dynamics simulations,[7–13] electric carrier simulations,[14,15] and atomic-scale simulations.[10,16–18] In these applications, the inputs and outputs of the machine learning model correspond to those of the computational simulations. Thus, faster computation is a major advantage of the surrogate model using machine learning. Another application of machine learning is to solve the reverse problem of simulations directly. Several researchers have reported machine learning
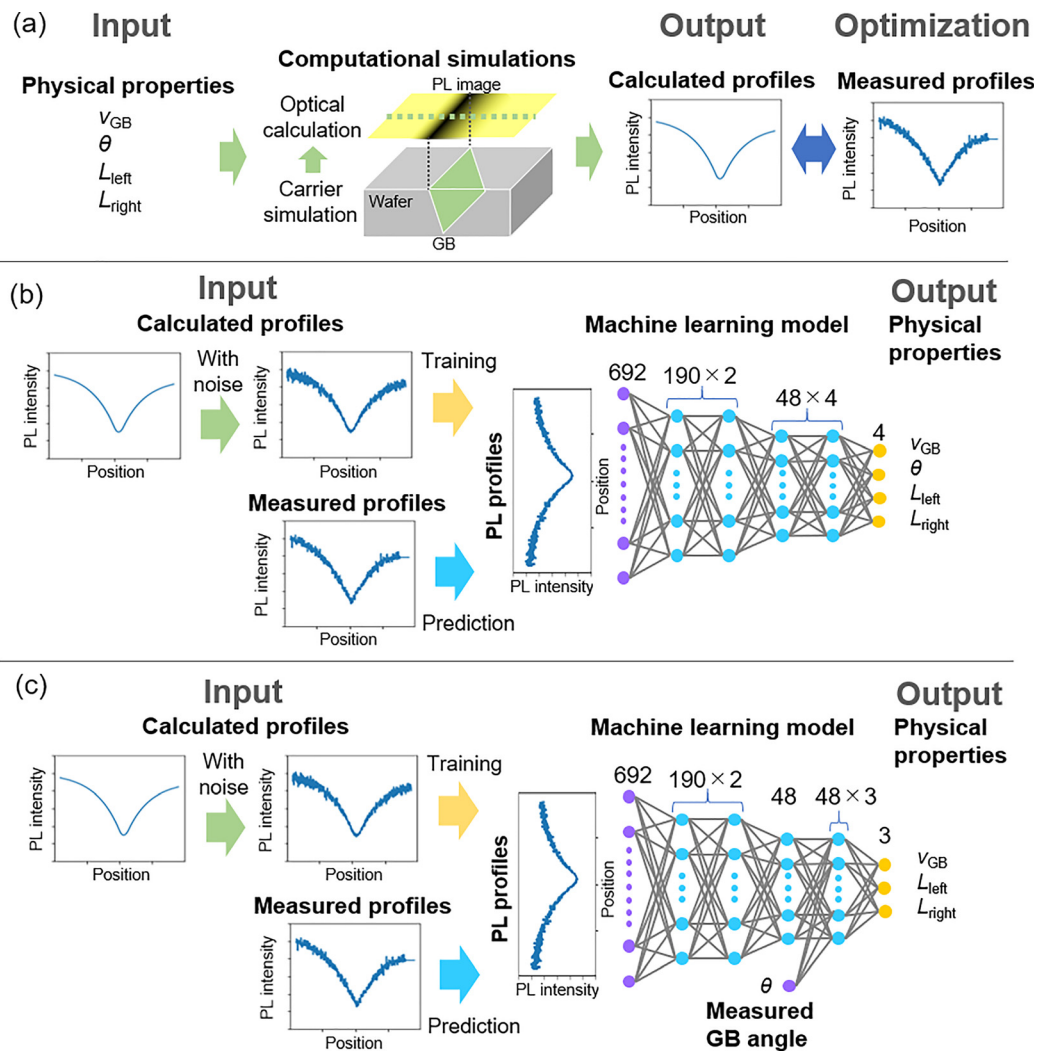
FIG. 1. Schematic of the evaluation of physical properties from a measured PL profile through a computational simulation and a machine learning model. (a) In the conventional evaluation process using simulations, the set of parameter values that best fit the measured values is explored via optimization methods, wherein the simulation calculations must be repeated. (b) In machine learning prediction, the physical property values can be obtained by a straightforward calculation through the model from the measured profile, where θ, the GB inclination angle, is the output parameter. (c) By adding the measurable parameter value, θ, as the input parameter of the machine learning model, the prediction accuracy will be increased.

applications in the device simulation of nanowires,[19] finite element method calculations for composite materials,[20] carrier lifetime simulation with the Shockley–Read–Hall equation,[21] and inverse ellipsometric problem.[22] Furthermore, Kiyohara *et al.* applied a machine learning model trained with simulation data to actual measurement data of a core-loss spectrum.[23]

In this study, we applied the above scheme to evaluate the physical properties, i.e., the carrier recombination velocity at a GB (v_{GB}), the GB inclination angle (θ), and the carrier diffusion length on the left and right sides of the grains (L_{right} and L_{left}, respectively), in multicrystalline Si from the PL intensity profile [Fig. 1(b)]. Multicrystalline Si is a major substrate material for solar cells, and it is expected to maintain a certain share because of the consumption of low-grade Si raw

materials produced in the material production and recycling as well as its effective cost-efficiency balance. GBs are one of the carrier recombination sites that affect solar cell efficiency, and their electrical activity varies widely depending on the structure.[24–26] However, the studied structure has been limited to simple structures, such as symmetric and straight boundaries. The electrical properties and atomic structure of curved boundaries, asymmetric boundaries, and locally reconstructed boundaries have a scientific interest. To study these GBs, a quantitative and spatially resolved evaluation method of analyzing v_{GB} continuously along the GB is necessary.[5] PL imaging is a nondestructive, non-contact, and highly spatially resolved measurement technique for GB characterization.[27–29] Recently, we developed a carrier simulation that considers the inclination of the GBs and proposed a quantitative

evaluation method of v_{GB} from a PL intensity profile using numerical optimization.[30] The issue of the continuous evaluation is the calculation time; the time required for optimization onto a measured PL profile was approximately 1 h. To reduce the computation time, we applied machine learning to the computational calculation results and analyzed the measured PL profile. Furthermore, we developed the machine learning model, in which the measurable parameter value, θ, is used as the input parameter, and we demonstrated improved prediction accuracy.

A PL intensity profile simulation was performed using a computational program built in-house based on the finite-difference method. First, the steady-state two-dimensional distribution of the excess carrier density around an inclined GB under uniform illumination for PL measurement was calculated. The spatial mesh size of the calculation model was $2.6 \mu m$, which was equal to the pixel resolution of the detector camera of the measurement system. The entire model size of the Si wafer was set to $3598.4 \times 182 \mu m^2$, which was adequately wide to ignore the influence of the side edges. The four variable parameters, v_{GB}, θ, L_{right}, and L_{left}, were incorporated in the calculation model as the boundary conditions, geometry parameters, and coefficients of the additional bulk carrier recombination in terms of the dominant carrier diffusion equation, respectively. Other physical properties, such as the surface carrier recombination velocity and carrier diffusion coefficient, were fixed in the simulations. Subsequently, the PL intensity profile across the GB was calculated by integrating the contribution from the excess carriers in each computational element with consideration of the optical defocusing of the measurement system. The total calculation time of the two sequential calculations was approximately 3 s using a workstation (specs is shown in Table S1 in the supplementary material). The details of the PL profile simulation are described in Ref. 30 and Fig. S2 in the supplementary material.

The dataset of simulation results for machine learning was produced with random values within the following range: $1.0 \times 10^1 \leq v_{GB} \leq 1.0 \times 10^6$ cm/s, $10 \leq \theta \leq 90°$, which implies that the GB inclines only to the right grain, $10 \leq L_{right}$ and $L_{left} \leq 1000 \mu m$. Considering the actual material property, a constraint in the range from >1/3 to <3 was set as the ratio between L_{right} and L_{left}. In addition, in actual samples, v_{GB} varied in a wide range, depending on the GB structures. Thus, for dataset generation and machine learning, v_{GB} was treated as a common logarithm, v_{log}, defined by $v_{log} = \log_{10} v_{GB}$. For machine learning, the values of the variables were standardized by the minimum and maximum values, and the calculated PL profiles were normalized by the maximum intensity.

To apply the machine learning model trained with the simulation data to the actual PL profile, the effect of noise in the measurement was adapted to the training data. We first evaluated the measurement noise from the standard deviation of the actual PL intensity in an area sufficiently far from the GBs. Divided by the average PL intensity in the area, the signal-to-noise ratio of our PL measurement, σ, was evaluated to be 0.035. This measurement noise originated mainly from the non-uniformity of the sample surface conditions and electrical noise of the detection camera. Thus, the noise was assumed to be proportional to the signal intensity. Artificial noise was generated from a standard normal distribution, $N(0, 1)$ (average = 0 and variance = 1). Subsequently, $(1 + \sigma N)$ was applied to the simulated PL profiles. Three thousand PL profiles with artificial noise were calculated and separated into 1800 training, 600 validation, and 600 testing datasets.

A fully connected feedforward neural network model was constructed and trained using the Keras[31] and Tensorflow[32] library in Python. The input of the model was the PL intensity profile vector data with 692 intensity values within $\pm 899.6 \mu m$ from the GB; the outputs were the four variables. The neural network architecture was optimized using the validation data and is shown in Fig. 1(b). A rectified linear unit (ReLU)[33] was applied to the activation function, and the loss was measured by the average of the mean squared error (MSE) for the outputs. For the model training, the learning rate and batch size were also optimized using the validation data, and a model checkpoint function that gives the model weights at the lowest validation loss during the training was used to avoid overfitting. For utilization of the measurable parameter of θ, its input position was examined using the validation data, and the best performance was obtained with the neural network structure shown in Fig. 1(c).
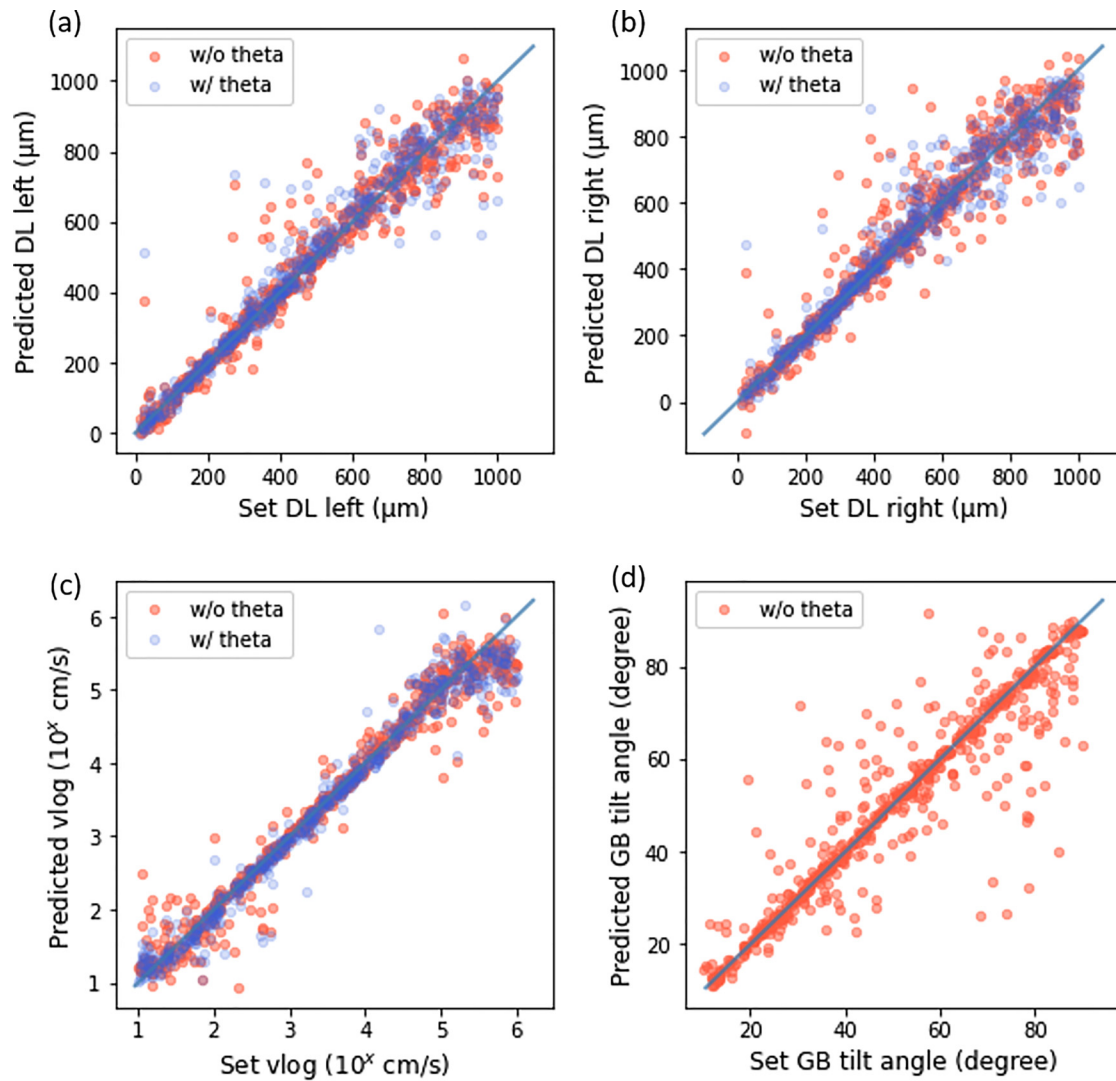
Figure 2 shows the relationship between the set and predicted values of the four variable parameters for the test dataset. The root mean squared error (RMSE) and R^2 score of the four parameters are summarized in Table I. The time required for neural network prediction is approximately 0.02 s. This time is much shorter than 1 h for the numerical optimization based on the simulation, in which approximately 66 iterations of the simulations for each 20 sets of initial parameter values are needed.

The obtained prediction accuracy is considerably high, but varies slightly with the parameters. L_{left} and v_{log} show relatively higher accuracies than the other two parameters. The prediction error of L_{right} is measurably larger than that of L_{left} owing to the GB inclination direction. In the simulations for the data generation, the zero position of the profile was set at the GB position on the front surface, and GB was inclined to the direction of the right-side grain within a range of θ. Under this GB configuration, the influence of the carrier recombination at GB and on the right-side grain overlapped each other. Thus, it was more difficult to obtain information about L_{right} from the PL profile compared to L_{left}.

In the parity plot of v_{log}, the data points are more widely distributed, i.e., the prediction error increases, in the value range of high and low values. This was caused by the decrease in sensitivity of the profile shape to the v_{log} value. Under the sample and measurement conditions simulated in this study, the change of the profile shape became significantly small at the extreme condition, $v_{log} < 10^2$ or $10^5 < v_{log}$, as demonstrated in Ref. 30. Thus, it was difficult to precisely determine v_{log} from the small change of the profile shape. For the same reason, the prediction accuracies of L_{right} and L_{left} decreased in their large value range.

The origin of the prediction errors discussed above is a general feature of carrier diffusion and recombination around the local defects in semiconductors. Thus, this is a common problem for conventional numerical fittings by repeating the PL profile simulation. This means that machine learning prediction will be useful as an alternative to conventional numerical fittings even though the prediction accuracy decreases under such extreme conditions.

In terms of the difference in the performance between the models with and without the measurable parameter of θ as the input parameter, the model with θ shows higher accuracy, especially in the prediction of v_{log}, as summarized in Table I. This suggests that applying additional information about the GB configuration is effective at improving the prediction accuracy.

FIG. 2. Relationship between the set and predicted values of the four parameters for the test dataset: (a) L_{left}, (b) L_{right}, (c) v_{log}, and (d) θ. Blue and red points show the results of the neural network structure with (w/) and without (w/o) θ as the input parameter. The straight lines in each figure demonstrate that the predicted value is equal to the set value. The results for the training dataset are shown in Fig. S4 in the supplementary material.

TABLE I. Prediction accuracy of the machine learning models for the four parameters for the test dataset. The values and errors show the average, maximum, and minimum in the results of 10 models trained with different initial weights. The model column shows the neural network structure with (w/) and without (w/o) θ as the input parameter. The results for the training dataset are summarized in Table S5 in the supplementary material.

Parameters	Model	RMSE	R^2
L_{left} (μm)	w/o θ	68.6 (+4.0, −4.2)	0.936 (+0.007, −0.006)
	w/ θ	62.4 (+5.0, −2.4)	0.945 (+0.004, −0.011)
L_{right} (μm)	w/o θ	82.0 (+2.8, −2.5)	0.900 (+0.009, −0.009)
	w/ θ	69.6 (+3.2, −4.8)	0.926 (+0.011, −0.010)
v_{log} (10^x cm/s)	w/o θ	0.284 (+0.015, −0.030)	0.960 (+0.008, −0.006)
	w/ θ	0.245 (+0.019, −0.015)	0.970 (+0.003, −0.004)
θ (°)	w/o θ	8.14 (+0.13, −0.20)	0.857 (+0.008, −0.006)

TABLE II. Results of conventional numerical fitting (CF) and machine learning prediction (ML) on the three actual PL profiles.

GB	Measured θ (°)	Method	L_{left} (μm)	L_{right} (μm)	v_{GB} (cm/s)
GB 1	90	ML	988	847	1952
		CF	538	509	1908
GB 2	75	ML	339	327	430
		CF	267	266	501
GB 3	66	ML	768	543	1701
		CF	502	439	1552

We performed conventional numerical fitting and machine learning prediction of the three parameters on three actual PL profiles that are the same ones examined in Ref. 30. The prediction and numerical fitting results are summarized in Table II. The v_{GB} values predicted by the machine learning model are almost equal to the results of the numerical fitting. Their difference is less than the prediction error of the machine learning shown in Table I. This finding supports the determination that the machine learning model is useful in characterizing v_{GB} of GBs.

On the other hand, the difference between the predicted and fitted values of the carrier diffusion length is larger than the prediction accuracy of the machine learning model shown in Table I, particularly in the prediction of large diffusion length GB. This is due to the error of not only the machine learning model but also the conventional fittings. As discussed above, the prediction accuracy of carrier diffusion length becomes low in the range of large values in both conventional numerical fitting and machine learning because of the sensitivity of PL intensity on the carrier diffusion length. Thus, the overlapped prediction error becomes considerably large in the large diffusion length range.

In addition, the measurement noise is not considered in the current simulation model for the numerical fitting, which certainly increases the prediction errors of the fittings on the actual profiles. In regard to the measurement noise, the machine learning model may, thus, be more effective than the conventional fittings.

Utilizing the high-speed direct prediction of v_{GB}, we conducted a continuous estimation of v_{GB} along a GB. Figure 3(a) shows a superimposed image of the distribution of v_{GB} on a PL image. One hundred and fifty PL intensity profiles across the GB were continuously extracted from the image, and v_{GB} at each position along the GB was predicted using the machine learning model. The total calculation time for the 150 profiles was approximately 3 s for the prediction and 1.7 h for the data generation and training. By contrast, it takes approximately 150 h to perform the conventional numerical fitting by standard methods. The calculation times are summarized in Table S3 in the supplementary material. v_{GB} was clearly visualized in the obtained distribution, and small fluctuations were detected quantitatively. v_{GB} increases around the curved region and fluctuates even in straight regions. This quantitative and high spatial resolution evaluation of the property will lead to a deep and quantitative understanding of defects by combining it with microscopic structural and computational analysis.

Here, we discuss the advantages, limitations, and further applications of machine learning as a solver of the reverse problem of the computational simulation for material evaluation. In addition to the substantial reduction in the computation time, as shown in Table S3 in the supplementary material, another significant advantage is the general versatility of the model. Once a model is constructed with simulation results, it can be used irrespective of wafers within the parameter range of the data in the training dataset. Note that a new dataset is necessary when the fixed parameters in the simulation change, for example, taking measurements using another system with different optical constants and wafers with different base doping concentration ranges. For the generation of the training data, simple random sampling is sufficient for practical use, and complicated optimization algorithms are not required. This makes installation and automation of the material evaluation simple. By contrast, conventional optimization must repeat the calculations in each evaluation, in which a sequential system with complicated algorithms and a long calculation time are necessary.

Another application is the preparation of the initial value conditions for conventional optimization. Global optimization through the machine learning model can provide appropriate initial value sets for optimization using simulation. This effectively reduces the calculation cost in the optimization.

The limitation of machine learning as a reverse problem solver is the presence of multiple roots. Although two or more parameter sets
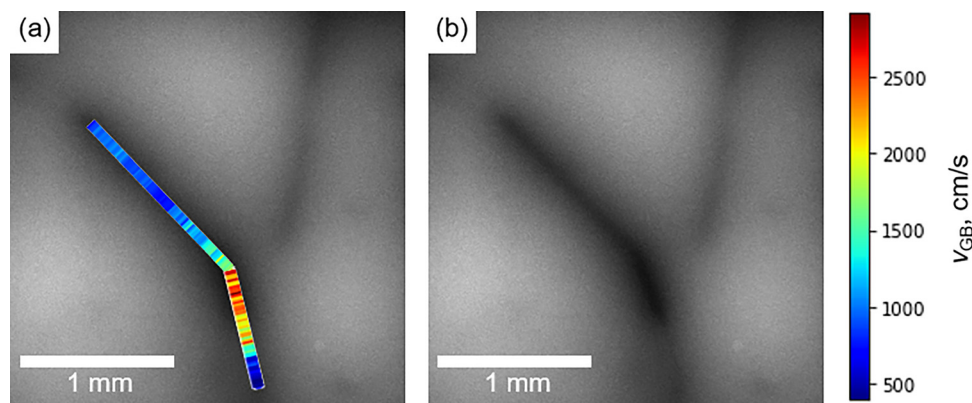
FIG. 3. (a) Distribution of v_{GB} along a GB superimposed on a PL image. v_{GB} corresponds to the velocity value shown in the color scale bar. (b) Original PL image.

represent the same simulation result, the machine learning model predicts only one of them. The PL intensity profile solved in this study changes almost monotonically with the parameters when θ is given as the measured value. Thus, the parameters are consistent with the measurements. For other applications, this limitation should be considered.

As demonstrated above, the proposed scheme to solve the reverse problem of the computational simulation can be a powerful tool to evaluate the spatial distribution of the material properties. By analyzing a number of PL profiles, continuous distribution of v_{GB} along a GB was obtained. In this case, PL profiles were extracted from the spatial distribution of carrier density using a PL measurement system. Similar to the carrier simulation performed in this study, the proposed method can be applied to any other simulations solving the governing differential equation, such as respective thermal, stress, and fluid simulations. For example, by applying machine learning to the simulation results of a temperature distribution around a boundary, thermal resistance across the boundary can be predicted, and its distribution along the boundary can be visualized.

In summary, we applied machine learning to solve the reverse problem of carrier and optical simulation of PL image measurement around an inclined GB in multicrystalline Si. The neural network model trained with 1800 simulated PL profiles with artificial noise had an R^2 score of 0.97 and RMSE of 0.245 for $v_{\log}$ prediction for the test dataset. The obtained accuracy of the prediction was sufficiently high for practical evaluation, and the calculation time to determine v_{GB} was significantly reduced compared to conventional optimization through repeated simulations. The three predicted parameters, L_{right}, L_{left}, and v_{GB}, for the actual PL profiles were consistent with those of conventional numerical fitting. This finding demonstrates the reliability of the neural network model. Furthermore, by conducting a fast quantitative evaluation through the proposed model, a continuous evaluation of v_{GB} was achieved. The fluctuation of v_{GB} along the GB was clearly visualized. This quantitative and high spatial resolution evaluation of v_{GB} will lead to an insightful quantitative understanding of GB physics.

The advantages, limitations, and further applications of the demonstrated machine learning model as a solver of the reverse problem of the computational simulation for material evaluation were discussed. The proposed model has an advantage of general versatility in addition to the drastically reduced computation time, while the presence of multiple roots should be considered as well. The method will be applicable to simulations solving the governing differential equation, such as carrier, thermal, and stress simulations. Owing to the considerably fast computation by the proposed machine learning model, prediction of the spatial distribution of physical properties will be accelerated.

See the supplementary material for computer specifications and calculation conditions, a schematic diagram of the simulation for the PL profile measurement, total calculation time of the conventional fitting and machine learning, and prediction accuracy for the training dataset.

DATA AVAILABILITY

The data that support the findings of this study are available from the corresponding author upon reasonable request.

REFERENCES

[1]J. Nocedal and S. J. Wright, *Numerical Optimization* (Springer, New York, 2006).
[2]R. H. Byrd, P. Lu, and J. Nocedal, SIAM J. Sci. Stat. Comput. **16**, 1190 (1995).
[3]C. Zhu, R. H. Byrd, and J. Nocedal, ACM Trans. Math. Software **23**, 550 (1997).
[4]M. Melanie, *An Introduction to Genetic Algorithms* (MIT Press, Cambridge, MA, 1996).
[5]B. Shahriari, K. Swersky, Z. Wang, R. P. Adams, and N. de Freitas, Proc. IEEE **104**, 148 (2016).
[6]Y. Jin, Swarm Evol. Comput. **1**, 61 (2011).
[7]N. Dropka and M. Holena, J. Cryst. Growth **471**, 53 (2017).
[8]Y. Tsunooka, N. Kokubo, G. Hatasa, S. Harada, M. Tagawa, and T. Ujihara, CrystEngCommun **20**, 6546 (2018).
[9]Y. Dang, L. Liu, and Z. Li, J. Cryst. Growth **522**, 195 (2019).
[10]Y. Ding, Y. Zhang, and Y. Ren, Chem. Eng. Res. Des. **151**, 131 (2019).
[11]Y. Takehara, A. Sekimoto, Y. Okano, T. Ujihara, and S. Dost, J. Cryst. Growth **532**, 125437 (2020).
[12]Y. Dang, C. Zhu, M. Ikumi, M. Takaishi, W. Yu, W. Huang, X. Liu, K. Kutsukake, S. Harada, M. Tagawa, and T. Ujihara, CrystEngComm **23**, 1982 (2021).
[13]W. Yu, C. Zhu, Y. Tsunooka, W. Huang, Y. Dang, K. Kutsukake, S. Harada, M. Tagawa, and T. Ujihara, CrystEngComm **23**, 2695 (2021).
[14]B. Rouet-Leduc, K. Barros, T. Lookman, and C. J. Humphreys, Sci. Rep. **6**, 24862 (2016).
[15]H. Wagner-Mohnsen and P. P. Altermatt, IEEE J. Photovoltaics **10**, 1441 (2020).
[16]J. Behler and M. Parrinello, Phys. Rev. Lett. **98**, 146401 (2007).
[17]T. Yokoi, Y. Noda, A. Nakamura, and K. Matsunaga, Phys. Rev. Mater. **4**, 014605 (2020).
[18]S. Fujii, T. Yokoi, C. A. J. Fisher, H. Morikawa, and M. Yoshiya, Nat. Commun. **11**, 1854 (2020).
[19]H. Carrillo-Nuñez, N. Dimitrova, A. Asenov, and V. Georgiev, IEEE Electron Device Lett. **40**, 1366 (2019).
[20]S. Ye, B. Li, Q. Li, H.-P. Zhao, and X.-Q. Feng, Appl. Phys. Lett. **115**, 161901 (2019).
[21]Y. Buratti, Q. T. Le Gia, J. Dick, Y. Zhu, and Z. Hameiri, npj Comput. Mater. **6**, 142 (2020).
[22]J. Liu, D. Zhang, D. Yu, M. Ren, and J. Xu, Light: Sci. Appl. **10**, 55 (2021).
[23]S. Kiyohara, K. Tsubaki, K. Liao, and T. Mizoguchi, J. Phys.: Mater. **2**, 024003 (2019).
[24]J. Chen and T. Sekiguchi, Jpn. J. Appl. Phys. **46**, 6489 (2007).
[25]K. Kutsukake, N. Usami, K. Fujiwara, Y. Nose, T. Sugawara, T. Shishido, and K. Nakajima, Mater. Trans. **48**, 143 (2007).
[26]T. Kojima, T. Tachibana, Y. Ohshita, R. R. Prakash, T. Sekiguchi, and M. Yamaguchi, Jpn. J. Appl. Phys. **54**, 08KD16 (2015).
[27]T. Trupke, R. A. Bardos, M. C. Schubert, and W. Warta, Appl. Phys. Lett. **89**, 044107 (2006).
[28]J. A. Giesecke, M. Kasemann, and W. Warta, J. Appl. Phys. **106**, 014907 (2009).
[29]H. C. Sio and D. Macdonald, Sol. Energy Mater. Sol. Cells **144**, 339 (2016).
[30]K. Mitamura, K. Kutsukake, T. Kojima, and N. Usami, J. Appl. Phys. **128**, 125103 (2020).
[31]See https://keras.io for "Keras" (last accessed June 5, 2021).
[32]See tensorflow.org for "Large-scale machine learning on heterogeneous systems," TensorFlow, 2015 (last accessed June 5, 2021).
[33]X. Glorot, A. Bordes, and Y. Bengio, in Proc. Mach. Learn. Res. **15**, 315 (2011); available at https://proceedings.mlr.press/v15/glorot11a.html.